Semi-Annual Report Submitted to the
National Aeronautics and Space Administration

For July - December, 1994

Contract Number: NAS5-31370

Land Surface Temperature Measurements from EOS MODIS Data

MODIS Team Member

ZHENGMING WAN
Institute for Computational Earth System Science
University of California, Santa Barbara

P.I.'s Address:

ZHENGMING WAN
Institute for Computational Earth System Science
University of California
Santa Barbara, CA 93106-3060

phone : (805) 893-4541
Fax no: (805) 893-2578
Internet: wan@icess.ucsb.edu

Land Surface Temperature Measurements from EOS MODIS Data

Semi-Annual Report
For July - December, 1994

Zhengming Wan, University of California at Santa Barbara

Contract Number: NAS5-31370

Abstract

A generalized split-window method for retrieving land-surface temperature (LST) from AVHRR and MODIS data has been developed. Accurate radiative transfer simulations show that the coefficients in the split-window algorithm for LST must depend on the viewing angle, if we are to achieve a LST accuracy of about 1 °K for the whole scan swath range (±55.4 ° and ±55° from nadir for AVHRR and MODIS, respectively) and for the ranges of surface temperature and atmospheric conditions over land, which are much wider than those over oceans. We obtain these coefficients from regression analysis of radiative transfer simulations, and we analyze sensitivity and error by using results from systematic radiative transfer simulations over wide ranges of surface temperature and emissivities, and atmospheric water vapor abundance and temperatures. Simulations indicated that as atmospheric column water vapor increases and viewing angle is larger than 45° it is necessary to optimize the split-window method by separating the ranges of the atmospheric column water vapor and lower boundary temperature, and the surface temperature into tractable sub-ranges. The atmospheric lower boundary temperature and (vertical) column water vapor values retrieved from HIRS/2 or MODIS atmospheric sounding channels can be used to determine the range where the optimum coefficients of the split-window method are given. This new LST algorithm not only retrieves LST more accurately but also is less sensitive than viewing-angle independent LST algorithms to the uncertainty in the band emissivities of the land-surface in the split-window and to the instrument noise.

The beta II version of the MODIS LST software was delivered in October. The version 2 of the MODIS LST ATBD (Algorithm Theoretical Base Document) was completed in December.

1. Work Accomplished

1.1. Band Emissivities of the Terrestrial Materials

In general, the band average emissivity defined by surface temperature T_s, spectral emissivity ε and the spectral response function of the sensor in this band $\Psi(\lambda)$,

$$\bar{\varepsilon} = \frac{\int_{\lambda_1}^{\lambda_2} \Psi(\lambda)\,\varepsilon(\lambda)\,B(\lambda, T_s)\,d\lambda}{\int_{\lambda_1}^{\lambda_2} \Psi(\lambda) B(\lambda, T_s)\,d\lambda} \tag{1}$$

is a function of the surface temperature. But in the earth surface environment, this temperature-dependence is usually very small. In an extreme example of coarse sands, the spectral emissivity increases by about 0.2 from the lower end to the upper end in AVHRR channel 3 at 3.75 μm, its band average emissivity changes only 0.004 as the temperature changes from 240 °K to 320 °K. Therefore, the Planck function term $B(\lambda, T)$ can be omitted without introducing any significant error in particular at wavelengths longer than 8 μm.

If a pixel consists of two components of land covers, one with ε_1 and surface temperature T_1, and the other with ε_2 and T_2, and proportions are p_1 and p_2, respectively, the average emissivity in band i will be

$$\varepsilon_i = \frac{\int_{\lambda_{(i,lower)}}^{\lambda_{(i,upper)}} \Psi(\lambda)\,[p_1\,\varepsilon_1(\lambda)\,B(\lambda, T_1) + p_2\,\varepsilon_2(\lambda)\,B(\lambda, T_2)]\,d\lambda}{\int_{\lambda_{(i,lower)}}^{\lambda_{(i,upper)}} \Psi(\lambda)\,[p_1\,B(\lambda, T_1) + p_2\,B(\lambda, T_2)]\,d\lambda} \tag{2}$$

The temperature effect on the band emissivity of a pixel mixed with two components (sandy soil and grass in this example) is shown in Table 1. The spectral response functions for NOAA-11 AVHRR bands 3, 4 and 5, and the specified response functions for MODIS bands 29, 31 and 32 are used in calculations. As shown in the first two rows, the band emissivity changes little even in the medium wavelength band, AVHRR band 3 at 3.75μm. However, if the two subpixel components have different emissivity values, the effective band emissivity not only varies with the proportions but also

with the temperature difference between two components. As T_2, the temperature of the second component changes to 285 °K from 300 °K, AVHRR band emissivity ε_3 changes up to 0.04 and MODIS band emissivity ε_{29} changes up to 0.009, but the band emissivity in the split window range changes less than 0.001. These numbers mean that the temperature effect on band emissivities in the split-window is negligible so that the IR radiation from a mixing pixel can be described by a single effective surface temperature and band emissivities, which are determined by proportions at a standard temperature (300 °K), in bands within the split-window (i.e, AVHRR bands 4 and 5, and MODIS bands 31 and 32). But this may be not the case for other bands at shorter wavelengths if there is a strong emissivity contrast within the pixel.

From the point of view of satellite remote sensing, the land surface is the top layer of the interface or biosphere between the lower boundary of the atmosphere and the solid earth. In the thermal infrared region, the thickness of this top layer is within a few millimeters. The entire Earth's land surface consists of evergreen forest and shrubs, deciduous forest and shrubs, crop and grass lands, inland water bodies, wetlands, glaciers, and ice/snow cover, barren and urban areas, bare soil, exposed bedrock, volcanic rocks, sands, shale and sediments. One of the major difficulties in development of LST algorithms is the considerable spectral variation in emissivities for different land-surface materials and for many of them, emissivities have been measured only for the spectrally integrated range from 8 to 14 μm [Griggs, 1968; Nerry et al., 1990; Salisbury and D'Aria, 1992; Rees, 1993]. Emissivity may also vary with the viewing angle [Dozier and Warren, 1982; Labed and Stoll, 1991; Rees and James, 1992], an effect that is more important over land than over water because the combination of surface slope and AVHRR scan angle routinely results in local viewing angles near 69 °. In laboratory measurements of bare soils, Labed and Stoll [1991] verified the angular effect and showed that this effect is smaller at wavelengths 10.6 and 12.0 μm than at 3.7 μm. Oblique viewing results in a shift of the signature, the spectral features being essentially unchanged. At viewing angle 60 °, this angular effect does not exceed 1.5% for sand and silty materials but it is up to about 5% for agricultural soils. Soil emissivity may vary with soil particle size [Salisbury and D'Aria, 1992]. And due to atmospheric effects, the emissivity spectra derived from field measurement and airborne sensor data may be different from the spectra derived from laboratory data [Rivard et al., 1993] if the atmospheric effect is not fully corrected. As is well known, the accurate determination of surface emissivity needs information about the surface BRDF. The conventional method to measure surface emissivity by using an integrating sphere assumes that the reference surface and a sample surface

have a similar BRDF pattern. Otherwise, the uncertainty in measured emissivity may be up to $\pm 5\%$ for IR spheres in cases of mixed diffuse and nondiffuse samples and reference [Hanssen, 1989]. In vegetation, the emitted radiation varies with the viewing angle, because of temperature structure in the vegetation canopy besides the angular effect in the surface emissivity [Kimes, 1981].

Despite all these variations mentioned above, there are evidences showing relatively stable spectral emissivity characteristics for terrestrial land covers in the wavelength range 10.5-12.5μm, where AVHRR bands 4 and 5, and MODIS bands 31 and 32 are located. And spectral contrast in surface emissivities usually decrease with aggregation as spatial scale increases. Salisbury and D'Aria [1992] published spectral reflectance data of 79 terrestrial material samples including igneous, metamorphic, and sedimentary fresh rocks; varnished rock surfaces, lichen-covered sandstone, soil samples, green foliage, senescent foliage, water ice, and water surfaces with suspended quartz sediment and oil slicks. The band average emissivities in MODIS bands 31 and 32 calculated from these reflectance spectra are shown in Figure 1.

In Figure 1. the solid line represents the grey body relation $\varepsilon_{31} = \varepsilon_{32}$ and the upper and lower dashed lines represent $\varepsilon_{32} - \varepsilon_{31} = 0.023$ and $\varepsilon_{32} - \varepsilon_{31} = -0.012$, respectively. We can gain the following insights into the band average emissivities of terrestrial materials: (1) all ε_{31} and ε_{32} are larger than 0.825; (2) a general relation $-0.012 \le \varepsilon_{32} - \varepsilon_{31} \le 0.023$ holds for all samples except fresh rocks, smooth surface of distilled water ice, and senescent beech foliage; and a narrower specific relation could be found for fresh foliage samples, senescent foliage samples, soil samples, varnished and lichen-covered rock samples, water and ice samples, respectively; (3) all ε_{31} and ε_{32} are larger than 0.91 for fresh foliage samples, soil samples, varnished and lichen-covered rock samples, water and ice samples; Besides, Salisbury and D'Aria [1992] also indicate that multiple scattering within the canopy of radiation emitted primarily by leaves will have its spectral contrast reduced and that after canopy scattering the typical tree, bush, and grass result in an emissivity quite close to 1. Field measurements of the true spectral emissivities of prairie grasses have shown an emissivity of 0.99 ± 0.01 [Palluconi et al., 1990]. In case of upright grass canopies, an angle of observation far from nadir may reduce scattering and emissivity [Norman et al., 1990]. After all, a constant emissivity approximation (in 0.96-0.98) in AVHRR band 5 (and as a consequence, the Lambertian surface approximation) is quite good for all natural land covers except for areas covered by exposed rocks and sands. Although more field measurements are needed to confirm this approximation, it is

quite safe to say that the band emissivities in AVHRR bands 4 and 5, and MODIS bands 31 and 32 are relatively stable and known within about 0.01 for dense evergreen canopies, lake surface, ice/snow covers, and most soils. Because their band emissivities are very close to the emissivities of water surface, the effect of rains is negligible for these land covers.

1.2. A Generalized LST Algorithm

1.2.1. Radiative Transfer Simulations

1.2.1.1. Ranges of the Simulation Space

It is important to make radiative transfer simulations for wide ranges of atmospheric and surface conditions. This is the advantage of the numerical experiments by using computers over real ground-based measurements which provide data coincident with satellite measurements for establishment of a statistical LST algorithm.

Accurate radiative transfer simulations have been made for 12 atmospheric temperature profiles, which cover the range of surface air temperatures, T_{air}, from 256 °K to 310 °K. It will be extended to 240-325 °K in the near future.

The water vapor profile was scaled from the near saturated level down to 5% of the saturated level for each temperature profile. The column water vapor is mainly limited by the atmospheric low boundary temperature to a few centimeters in cold atmospheric conditions and to more than 5cm in warm tropical atmospheric conditions. Totally, 125 atmospheric conditions with different temperature and/or water vapor profiles are used in radiative transfer simulations.

The land-surface temperature, T_s, ranges from $T_{air} - 16$ °K to $T_{air} + 16$ °K. This range may be extended or reduced if necessary after enough LST values are retrieved in the global scale. This wide range will be split into two overlapped sub-ranges, one from -2 to +16 °K, another from -16 to +2 °K for the reason described later.

According to Figure 1, we consider surface emissivity variations of natural land covers in two sub-groups, one defined by $0.96 \le \varepsilon_5 \le 1.0$ and $-0.025 \le \varepsilon_4 - \varepsilon_5 \le 0.015$, and another defined by $0.91 \le \varepsilon_5 \le 0.95$ and $-0.025 \le \varepsilon_4 - \varepsilon_5 \le 0.015$. The first group represents the band emissivity conditions for most land covers at viewing angles up to 45 ° from nadir. The second group represents the conditions for larger viewing angles.

An accurate atmospheric radiative transfer code has been developed for more than ten years on different workstations including IBM RISC/6000, and DEC 3000 Model 800 Alpha workstations. It takes about 3 hours of CPU time on the DEC 3000/800 Alpha workstation to make a complete simulation for one atmospheric temperature and water vapor condition over the spectral range 775-1000cm^{-1} in the spectral interval of 5cm^{-1} for a series of surface emissivity and temperature conditions. The exponential-sum tables derived from LOWTRAN-7 transmission functions are used in simulations to obtain results used in this paper. In the spectral range 775-1000cm^{-1}, the numerical monochromatic radiative transfer equation is solved for 1,000-8,600 times in each spectral interval in order to deal with the molecular band absorptions of H2O, CO2 and O3. Recently, this radiative transfer code has been ported to Cary T3d, one of the High Performance Computing and Communications (HPCC) testbeds. The computational speed increases with the number of nodes at an efficiency of 90% on this parallel computing system.

1.2.1.2. Numerical Model of IR Remote Sensing

According to results from accurate radiative transfer simulations for given conditions of atmospheric profiles and a Lambertian land surface, the thermal infrared spectral signature measured from satellite-borne sensors may be expressed as [Wan and Dozier, 1990]

$$L(j) = t_1(j)\,\varepsilon(j)\,B(j, T_s) + \frac{1-\varepsilon(j)}{\pi}\,[t_2(j)\,E_a(j) + t_3(j)\,E_s(j)] + L_a(j) + L_s(j) \qquad (3)$$

here $\varepsilon(j)$ is the band-average emissivity, $t_i(j)$, $i = 1, 2, 3$ are three effective band transmission functions for band j: for surface thermal emittance, atmospheric downward thermal irradiance reflected by the surface, and solar irradiance reflected by the surface, respectively. L_a is the atmospheric upward thermal radiance, and L_s is path radiance resulting from scattering of solar radiation. In general, these three effective band transmission functions are different due to the wavelength-dependent selective effect of the molecular band absorption.

1.2.2. Viewing-angle Dependent LST Algorithm

Based on a series of accurate radiative transfer simulations, we present a generalized split-window algorithm for retrieving land-surface temperature from space, specifically using NOAA-11 AVHRR data in following sections. Becker and Li [1990] presented a split-window LST algorithm for viewing angles up to 46 ° from nadir in form of

$$T_s = A_0 + P\frac{T_4 + T_5}{2} + M\frac{T_4 - T_5}{2} \tag{4}$$

For NOAA-11 AVHRR, the coefficients are [Li and Becker, 1993]

$$A_0 = 1.274$$

$$P = 1 + 0.15616\frac{1-\varepsilon}{\varepsilon} - 0.482\frac{\Delta\varepsilon}{\varepsilon^2}$$

$$M = 6.26 + 3.98\frac{1-\varepsilon}{\varepsilon} + 38.33\frac{\Delta\varepsilon}{\varepsilon^2}$$

where $\varepsilon = 0.5(\varepsilon_4 + \varepsilon_5)$, and $\Delta\varepsilon = \varepsilon_4 - \varepsilon_5$.

Since the maximum viewing angle for AVHRR sensors is 68.97° from nadir, pixels with viewing angle larger than 46° account for nearly 30% of the total pixels, or almost 50% of the total coverage area within each swath. We have to develop a LST algorithm for the whole viewing angle range in order to provide a global coverage for LST. Although a LST algorithm in a quadratic form of combinations of μ, the cosine of the viewing angle, and TIR band brightness temperatures [Wan and Dozier, 1989] gives a better accuracy in cases where surface emissivity characteristics is well known, it may be very sensitive to uncertainties in emissivity characteristics and noises in band radiance data due to possible subpixel broken clouds. In the following, we will use a linear form for the LST algorithm

$$T_s = C + (A_1 + A_2\frac{1-\varepsilon}{\varepsilon} + A_3\frac{\Delta\varepsilon}{\varepsilon^2})\frac{T_4 + T_5}{2} + (B_1 + B_2\frac{1-\varepsilon}{\varepsilon} + B_3\frac{\Delta\varepsilon}{\varepsilon^2})\frac{T_4 - T_5}{2}, \tag{5}$$

where A_1 is not fixed at 1 so that there are one more variable coefficient in this form than in Becker and Li's algorithm. We have examined the viewing angle effect by comparing the accuracies of the viewing-angle (θ_v) independent algorithm with the θ_v- dependent algorithm. In the θ_v-independent algorithm, coefficients are obtained by regression analysis of simulation data sampled from the whole θ_v range. In the θ_v-dependent algorithm, coefficients are obtained by regression analysis of simulation data at individual viewing angles. Table 2 shows the RMS of LST errors followed by its maximum errors in the parentheses of these two split-window LST algorithms in different ranges of band emissivities and surface temperatures in cold and dry atmospheric conditions. The atmospheric low boundary temperature, i.e., T_{air-sf}, ranges from 256°K to 287°K, and atmospheric vertical column water vapor (i.e., in the nadir direction) ranges from almost 0 to 2cm. The upper half portion is for the first emissivity group with higher band emissivities, and the lower half portion for the

second emissivity group. The first row in each portion gives RMS and maximum errors in these two method at viewing angles 69°, 45° and 0°, respectively, for algorithms which coefficients are obtained by regression analysis of data for the whole surface temperature range ±16 °K from T_{air-sf}. Although the θ_v independent and dependent algorithms gives almost same maximum errors, the RMS errors in the θ_v-dependent is much smaller at all viewing angles. Since the maximum error is larger than 4 °K even in the θ_v-dependent algorithm, we tried LST iterations once and twice. In the first LST iteration, we used LST coefficients for the two T_s sub-ranges, one from -2 to +16 °K, another from -16 to +2 °K. The retrieved T_s value is used to determine which sub-range should be used in the first iteration. If the surface temperature is within its upper sub-range, both RMS and maximum errors can be significantly reduced. If the surface temperature is within its lower sub-range, no improvement can be made due to the low TIR signature from the surface. If we divide the T_s range into 4 sub-ranges, second iteration can be made to improve the LST accuracy in some sub-ranges. In this way, the θ_v-dependent algorithm improves the LST accuracy by a factor from 1 to 3.

The θ_v-dependent LST algorithm is better than θ_v-independent algorithms due to the factor that the optical depth along viewing angle 69° is more than twice the optical depth in the vertical direction. As atmospheric vertical column water vapor is larger than 4.5cm, the atmospheric transmission function reduces by a factor of 3 from nadir to viewing angle 69° in AVHRR band 4, and by a factor of 4 in AVHRR band 5. The θ_v-dependent algorithm will be the only choice to retrieve LST at an accuracy of the 1 °K level.

1.2.3. Using Column Water Vapor in the θ_v-dependent LST Algorithm

As indicated in Table 2, although the RMS LST error is smaller than 1 °K the maximum LST error exceeds 2 °K and 3.5 °K at viewing angles 45° and 69 °K respectively, even the θ_v-dependent LST algorithm is iteratedly used. We can significantly improved the LST accuracy by separate the column water vapor range into 1cm or 0.5cm intervals. The impacts of using the water vapor information in θ_v independent and dependent algorithms on the LST accuracy are shown in Table 3. Results in this table are obtained by a systematic error analysis of the two LST algorithms developed for different sizes of its application ranges. The smallest total number of the simulated observations used to make regression analysis for producing the LST coefficients A_i, B_i and C in Equation (12) is 4650. The accuracy of the θ_v-independent LST algorithm is only slightly improved by using the column water vapor information. However, the accuracy of the θ_v-dependent LST algorithm has

been dramatically improved by the column water vapor information. With iteration once of the 1cm-interval θ_v-dependent algorithm, the RMS error does not exceed 0.7 °K and the maximum error does not exceed 3 °K even at the largest viewing angle. If the LST algorithm for column water vapor intervals of 0.5cm is used, the RMS error does not exceed 0.51 °K and the maximum error does not exceed 1.7 °K at viewing angle 69 °. In the viewing angle range up to 45 °, the RMS error does not exceed 0.27 °K and the maximum error does not exceed 0.91 °K. Figure 2 shows the viewing angle dependence of the RMS and maximum LST errors of the θ_v-dependent algorithm in cold and dry atmospheric conditions ($T_{air-sf} \leq 287.2$ °K, column water vapor in 1-2cm).

1.2.4. Using Atmospheric Lower Boundary Temperature in the θ_v-dependent LST Algorithm

As column water vapor in a tropical atmosphere is larger than 4cm, the atmospheric transmission functions in AVHRR bands 4 and 5 reduce to 0.22 and 0.12, respectively, LST retrieval from satellite TIR data becomes difficult at large viewing angles. In order to get a quantitative assessment of the retrieved LST accuracy, we developed two sets of θ_v-dependent algorithms for two ranges of the atmospheric lower boundary temperature, one is from 300 °K to 310 °K, another is from 300 °K to 305 °K. Corresponding RMS and maximum errors are shown in Table 4 for the higher emissivity group, and in Table 5 for the lower emissivity group. The last column indicates the maximum temperature deficit, i.e., the difference between surface temperature T_s and the brightness temperature in AVHRR band 4, T_4. When column water vapor is less than 4cm, the two sets of LST algorithms have almost the same accuracy. When column water vapor is larger than 4cm, the maximum temperature deficit may be larger than 27 °K. The RMS and maximum error of the LST algorithm for the wider T_{air-sf} range may be larger than 1 °K and 3.8 °K, respectively. The maximum LST error can be reduced by 1-2 °K if the 300-305 °K LST algorithm is used. Figure 3 shows the viewing angle dependence of the RMS and maximum LST errors of the θ_v-dependent algorithm in warm atmospheric conditions ($300\ °K \leq T_{air-sf} \leq 305$ °K, column water vapor in 3.4-4cm) for the higher emissivity group.

1.2.5. Sensitivity Analysis

A better LST algorithm should have at least the following two features: (1) it retrieves LST more accurately; (2) it is not very sensitive to uncertainties in our knowledge of surface emissivities and atmospheric properties, and to the instrument noises. So far we have seen that the θ_v-dependent generalized split-window LST algorithm retrieves LST more accurately than θ_v-independent LST

algorithms. Now we turn to analize its sensitivity to uncertainties in surface emissivities. According to Equation (5), the factors on the emissivity terms $(1-\varepsilon)/\varepsilon$ and $\Delta\varepsilon/(\varepsilon^2)$ are

$$\alpha = A_2 \frac{T_4+T_5}{2} + B_2 \frac{T_4-T_5}{2} \tag{6-a}$$

and

$$\beta = A_3 \frac{T_4+T_5}{2} + B_3 \frac{T_4-T_5}{2} \tag{6-b}$$

respectively. Table 6 shows the maximum values of α and β in the θ_v independent and dependent LST algorithms in cold and dry atmospheric conditions. There is no any significant difference in maximum α values of these two LST algorithms. But the maximum β values are very different. Over the column water vapor sub-range 0.5-1cm, max (β) values in the θ_v-independent LST algorithm are 157 and 147 in the higher and lower emissivity groups, respectively, at the nadir viewing direction. They are larger than twice the values in the θ_v-dependent algorithm. This means that the θ_v-independent algorithm will have a LST error up to 1.6 °K if there is an uncertainty of 0.01 in the value of $\Delta\varepsilon/(\varepsilon^2)$. We expect that this uncertainty is around 0.005 for well known land surfaces such as dense vegetation, snow/ice covers and lake surface. It will result in a LST error up to 0.8 °K if the θ_v-independent algorithm is used. The θ_v-dependent algorithm is much less sensitive to the value $\Delta\varepsilon/(\varepsilon^2)$, giving this kind of maximum LST error around 0.37 °K at the nadir viewing direction. The view angle dependences of the emissivity sensitivities for these two algorithms are shown in Figure 4. Similarly, Table 7 and Figure 5 show the maximum emissivity sensitivities in warm atmospheric conditions, $294\,°K \le T_{air-sf} \le 300\,°K$. As expected, all LST algorithms are more sensitive to the uncertainty in $\Delta\varepsilon$ in dry atmospheric conditions. This sensitivity decreases as atmospheric column water vapor is larger due to the compensative effect of the reflected downward atmospheric thermal infrared radiation.

In order to investigate the sensitivity of the θ_v-dependent LST algorithm to the instrument noise, we simulate the instrument noise by synthetic quantization. We suppose the radiance values of AVHRR bands 4 and 5 to saturate at temperature 325 °K. The quantization step is calculated by 10 bits. The radiance values are expressed by a 10-bit integer through the synthetic quantization and then converted to double precision floating point number by multiplying the quantization step. Compare the RMS and maximum LST errors by apply the same θ_v-dependent algorithm to the original

simulation data and the data through the synthetic quantization. We change 10 bits to 9 bits and make a similar comparison. The differences in RMS and maximum errors due to quantizations using 10 and 9 bits are shown in Table 8. Note that all viewing angles up to 69° are included in this analysis. These results show that the θ_v-dependent LST algorithm is quite stable to the 10-bit AVHRR data. It will be more stable to the 12-bit MODIS data.

1.2.6. Some Procedural Considerations

1.2.6.1. Programming of the θ_v-dependent LST Algorithm

Although it needs a lot of computer time to establish a complete hierarchical θ_v-dependent LST algorithm, the algorithm itself is still very simple and efficient to use. Once it is established, its coefficients are given in a multi-dimensional look-up table. As shown in Figure 6, the coefficients of the LST algorithm vary smoothly with viewing angle. Therefore, it is enough to keep in the look-up table only coefficients at no more than 10 viewing angles. The coefficients at any viewing angle can be interpolated from values of these coefficients in the look-up table. The calibrated TIR band radiance data can be easily converted to band brightness temperature values by using look-up tables at an accuracy better than the sensor's NEΔT (noise equivalent differential temperature).

1.2.6.2. LST Production

LST production consists of the following steps.

Cloud Masking, Cloudy pixels are detected and skipped in the LST production.

Estimation of Atmospheric Column Water Vapor and Lower Boundary Temperature, The atmospheric column water vapor and lower boundary temperature estimated from regional and seasonal climatological data [Dozier and Wan, 1994] are useful if we separate the entire simulation space into broad sub ranges. The atmospheric column water vapor and lower boundary temperature retrieved from NOAA HIRS/2 data can be used better in the LST algorithm for AVHRR data. But we can not expect an accurate column water vapor value to be used in the LST algorithm because HIRS/2 has a coarser spatial resolution than AVHRR and the spatial variation in atmospheric water vapor may be large. The θ_v-dependent LST algorithm proposed in this paper will be very suitable to MODIS data because MODIS has almost all the channels in AVHRR and HIRS/2 at the same 1km resolution. As indicated in the previous section, the atmospheric column water vapor and lower boundary

temperature retrieved from MODIS atmospheric sounding channels can significantly improve the LST accuracy especially in wet atmospheric conditions and at large viewing angles.

Land-surface Types and Fractional Vegetation Cover, The VNIR channels of AVHRR and MODIS can be used to estimate land-surface types and to derive the normalized difference vegetation index (NDVI). If we know the land-surface type of a pixel is fully dense vegetation, snow/ice cover, or water surface, then the band emissivities in AVHRR bands 4 and 5, or similarly in MODIS bands 31 and 32 can be estimated through an a priori emissivity knowledge base as shown in Figure 1. In arid and semiarid areas, vegetation cover can be sparse and may also evolve rapidly with time. Therefore, surface emissivity may be different from one pixel to another. Kerr et al. [1992] show that the fractional vegetation cover coefficient C can be estimated from the NDVI values with the expression

$$C = \frac{\mathrm{NDVI} - \mathrm{NDVI}_{bs}}{\mathrm{NDVI}_{v} - \mathrm{NDVI}_{bs}} \tag{7}$$

where NDVI_{bs} is the minimum value of the NDVI for bare soil over the area of interest and NDVI_{v} corresponds to the highest NDVI you can expect for a fully vegetated pixel (typically by the end of the rain season). It is possible to estimate band emissivities of bare soils based soil types from image classification (and soil maps if available). Finally, band emissivities can be estimated from fractional vegetation cover values pixel by pixel. Once band emissivities are known, LST can be retrieved.

1.3. Beta Delivery II of the MODIS LST Software

The beta II version of the MODIS LST software was delivered in October. This prototype MODIS LST algorithm has been developed from accurate radiative transfer simulations of MODIS data for retrieving surface temperature and band emissivities by using a look-up table method.

1.4. The Second Version of MODIS LST ATBD

In response to the written comments from peer reviewers and the review panel, some major changes were made in the MODIS LST ATBD. A generalized spli-window algorithm has been specified for the MODIS LST. The coefficients of the LST algorithm depend on viewing angle, and the ranges of atmospheric column water vapor and lower boundary temperature. New look-up table methods have been developed to retrieve surface band emissivities by using temporal or spatial features in TIR data so that the surface emissivity can be changed to at-launch parameter from post-launch parameter

which was originally planned in the first LST ATBD. The second version of the MODIS LST ATBD was completed and submitted to the EOS Project Office in December.

2. Anticipated Future Actions

The new LST algorithm will be validated and refined.

3. Publications

1. S. W. Running, C. O. Justice, V. Salomonson, D. Hall, J. Barker, Y. Kaufman, A. Strahler, A. Huete, J.-P. Muller, V. Vanderbilt, Z. Wan, and P. Teillet, Terrestrial remote sensing science and algorithms planned for EOS MODIS, temperature from EOS/MODIS data, *International Journal of Remote Sensing,* Vol. 15, No. 17, pp. 3587-3620, 1994.

2. Z. Wan, and J. Dozier, A generalized split-window algorithm for retrieving land-surface temperature from space, *IEEE Trans. Geosci. Remote Sens.* submitted January 1995.

REFERENCES

Becker, F. and Z. L. Li, "Toward a local split window method over land surface," *Intl. J. Remote Sens.*, vol. 3, pp. 369-393, 1990.

Dozier, J. and Z. Wan, "Development of practical multiband algorithms for estimating land-surface temperature from EOS/MODIS data," *Adv. Space Res.*, vol. 13, no. 3, pp. 81-90, 1994.

Dozier, J. and S. G. Warren, "Effect of viewing angle on the infrared brightness temperature of snow," *Water Resour. Res.*, vol. 18, no. 5, pp. 1424-1434, 1982.

Griggs, M., "Emissivities of natural surfaces in the 8- to 14-micron spectral region," *J. Geophys. Res.*, vol. 73, pp. 7545-7551, 1968.

Hanssen, L. M., "Effects of restricting the detector field of view when using integrating spheres," *Appl. Optics*, vol. 28, no. 11, pp. 2097-2103, 1989.

Kerr, Y. H., J. P. Lagouarde, and J. Imbernon, "Accurate land surface temperature retrieval from AVHRR data with use of an improved split window algorithm," *Remote Sens. Environ.*, vol. 41, no. 2-3, pp. 197-209, 1992.

Kimes, D. S., "Azimuthal radiometric temperature measurements of wheat canopies," *Appl. Optics*, vol. 20, no. 7, pp. 1119-1121, 1981.

Labed, J. and M. P. Stoll, "Angular variation of land surface spectral emissivity in the thermal infrared: laboratory investigations on bare soils," *Intl. J. Remote Sens.*, vol. 12, no. 11, pp. 2299-2310, 1991.

Li, Z. L. and F. Becker, "Feasibility of land surface temperature and emissivity determination from AVHRR data," *Remote Sens. Environ.*, vol. 43, pp. 67-85, 1993.

Nerry, F., J. Labed, and M. P. Stoll, "Spectral properties of land surfaces in the thermal infrared 1. laboratory measurements of absolute spectral emissivity signatures," *J. Geophys. Res.*, vol. 95, no. B5, pp. 7027-7044, 1990.

Norman, J. M., J. Chen, and N. Goel, "Thermal emissivity and infrared temperature dependency of plant canopy architecture and view angle," *Proceedings IGARSS '90*, pp. 1747-1750, 1990.

Palluconi, F., A. B. Kahle, G. Hoover, and J. E. Conel, "The spectral emissivity of prairie and pasture grasses at Konza Prairie, Kansas," in *Symposium on FIFE*, pp. 77-78, Boston, MA: American Meteorological Society, 1990.

Rees, W. G., "Infrared emissivities of Arctic land cover types," *Int. J. Remote Sensing*, vol. 14, pp. 1013-1017, 1993.

Rees, W. G. and S. P. James, "Angular variation of the infrared emissivity of ice and water surfaces," *Int. J. Remote Sensing*, vol. 13, pp. 2873-2886, 1992.

Rivard, B., S. B. Petroy, and J. R. Miller, "Measured effects of desert varnish on mid-infrared spectra of weathered rocks as an aid to TIMS imagery interpretation," *IEEE Trans. Geosci. Remote Sens.*, vol. 31, no. 1, pp. 284-291, 1993.

Salisbury, J. W. and D. M. D'Aria, "Emissivity of terrestrial materials in the 8-14 μm atmospheric window," *Remote Sens. Environ.*, vol. 42, pp. 83-106, 1992.

Salisbury, J. W. and D. M. D'Aria, "Infrared (8-14 μm) remote sensing of soil particle size," *Remote Sens. Environ.*, vol. 42, pp. 157-165, 1992.

Wan, Z. and J. Dozier, "Effects of the atmosphere and surface emissivity on the thermal infrared spectral signature measured from MODIS-N," *Proceedings IGARSS '90*, pp. 189-192, 1990.

Wan, Z. and J. Dozier, "Land-surface temperature measurement from space: physical principles and inverse modeling," *IEEE Trans. Geosci. Remote Sens.*, vol. 27, no. 3, pp. 268-278, 1989.

TABLE 1. The temperature effect on band emissivities of a pixel mixed with two components (sandy soil and grass) in NOAA-11 AVHRR and EOS MODIS bands. Bandwidths for NOAA-11 AVHRR bands 3, 4, and 5 are 3.54-3.94μm, 10.32-11.32μm, and 11.41-12.38μm, respectively. Bandwidths for MODIS bands 29, 31 and 32 are 8.4-8.7μm, 10.78-11.27μm, and 11.77-12.27μm, respectively.

mixing pixel parameters				AVHRR band			MODIS band		
p_1	T_1	p_2	T_2	ε_3	ε_4	ε_5	ε_{29}	ε_{31}	ε_{32}
1.0	273 °K	0.0	273 °K	0.7183	0.9533	0.9706	0.8612	0.9554	0.9766
1.0	300 °K	0.0	300 °K	0.7190	0.9532	0.9705	0.8611	0.9554	0.9765
0.75	300 °K	0.25	300 °K	0.7810	0.9555	0.9719	0.8900	0.9579	0.9768
0.5	300 °K	0.5	300 °K	0.8431	0.9577	0.9732	0.9189	0.9605	0.9771
0.25	300 °K	0.75	300 °K	0.9051	0.9600	0.9745	0.9478	0.9630	0.9773
0.0	300 °K	1.0	300 °K	0.9672	0.9623	0.9759	0.9767	0.9656	0.9776
0.75	300 °K	0.25	300 °K	0.7810	0.9555	0.9719	0.8900	0.9579	0.9768
0.75	300 °K	0.25	285 °K	0.7551	0.9551	0.9716	0.8841	0.9575	0.9768
0.75	300 °K	0.25	275 °K	0.7425	0.9549	0.9715	0.8803	0.9573	0.9767
0.5	300 °K	0.5	300 °K	0.8431	0.9577	0.9732	0.9189	0.9605	0.9771
0.5	300 °K	0.5	285 °K	0.8030	0.9572	0.9729	0.9104	0.9599	0.9770
0.5	300 °K	0.5	275 °K	0.7783	0.9568	0.9727	0.9044	0.9595	0.9770
0.25	300 °K	0.75	300 °K	0.9051	0.9600	0.9745	0.9478	0.9630	0.9773
0.25	300 °K	0.75	285 °K	0.8692	0.9596	0.9743	0.9409	0.9626	0.9773
0.25	300 °K	0.75	275 °K	0.8394	0.9593	0.9741	0.9354	0.9622	0.9773

TABLE 2. Error analysis of split-window LST algorithms in cold and dry atmospheric conditions ($T_{air-sf} \leq 287.2$ °K and vertical column water vapor < 2cm).

application ranges			θ_V-independent LST method			θ_V-dependent LST method			iteration
vwv (cm)	ε_5	$T_s - T_{air-sf}$	$\theta_V = 69°$	$\theta_V = 45°$	$\theta_V = 0°$	$\theta_V = 69°$	$\theta_V = 45°$	$\theta_V = 0°$	number
0 - 2	.96-1.0	-16 to +16	1.0 (4.5)	.42 (2.5)	.51 (2.0)	.62 (4.2)	.36 (2.5)	.29 (2.1)	0
0 - 2	.96-1.0	-2 to +16	1.1 (2.3)	.36 (1.8)	.56 (1.7)	.34 (2.2)	.23 (1.4)	.21 (1.2)	1
0 - 2	.96-1.0	-16 to +2	.86 (4.3)	.40 (2.3)	.39 (1.8)	.71 (4.1)	.39 (2.4)	.30 (1.9)	1
0 - 2	.96-1.0	+7 to +16	1.2 (2.1)	.38 (1.5)	.61 (1.6)	.25 (1.0)	.19 (.83)	.18 (.77)	2
0 - 2	.96-1.0	-2 to +9.5	.93 (1.9)	.31 (1.6)	.49 (1.6)	.29 (1.8)	.20 (1.2)	.18 (1.1)	2
0 - 2	.96-1.0	-9.5 to +2	.77 (2.8)	.30 (1.9)	.38 (1.6)	.44 (2.8)	.25 (1.7)	.21 (1.4)	2
0 - 2	.96-1.0	-16 to -7	.88 (4.1)	.47 (2.2)	.38 (1.6)	.86 (4.0)	.46 (2.2)	.36 (1.8)	2
0 - 2	.91-.95	-16 to +16	1.0 (5.1)	.47 (2.8)	.52 (2.1)	.73 (4.8)	.43 (2.9)	.36 (2.4)	0
0 - 2	.91-.95	-2 to +16	1.0 (2.6)	.39 (2.2)	.55 (2.0)	.40 (2.8)	.27 (1.8)	.23 (1.6)	1
0 - 2	.91-.95	-16 to +2	.93 (4.8)	.48 (2.4)	.43 (1.7)	.86 (4.5)	.48 (2.4)	.39 (2.0)	1
0 - 2	.91-.95	+7 to +16	1.1 (2.1)	.39 (1.8)	.60 (1.9)	.27 (1.5)	.22 (1.2)	.20 (1.1)	2
0 - 2	.91-.95	-2 to +9.5	.91 (2.3)	.34 (2.0)	.48 (1.8)	.37 (2.4)	.25 (1.6)	.21 (1.4)	2
0 - 2	.91-.95	-9.5 to +2	.81 (3.6)	.40 (2.3)	.41 (1.9)	.56 (3.3)	.39 (2.3)	.33 (1.9)	2
0 - 2	.91-.95	-16 to -7	.94 (4.2)	.48 (1.8)	.42 (1.5)	.90 (3.7)	.48 (1.9)	.40 (1.5)	2

TABLE 3. The improvement of split-window LST algorithms in cold and dry atmospheric conditions ($T_{air-sf} \leq 287.2$ °K and vertical column water vapor < 2cm) by using the water vapor information.

application ranges			θ_V-independent LST method			θ_V-dependent LST method			iteration
vwv (cm)	ε_5	$T_s - T_{air-sf}$	$\theta_V = 69°$	$\theta_V = 45°$	$\theta_V = 0°$	$\theta_V = 69°$	$\theta_V = 45°$	$\theta_V = 0°$	number
0 - 1	.96-1.0	-16 to +16	.84 (1.9)	.23 (.96)	.44 (1.2)	.59 (1.7)	.15 (.92)	.13 (.81)	0
0 - 1	.96-1.0	-2 to +16	.99 (1.8)	.26 (.83)	.51 (1.1)	.14 (.79)	.12 (.53)	.12 (.50)	1
0 - 1	.96-1.0	-16 to +2	.58 (1.3)	.16 (.78)	.29 (.83)	.21 (1.2)	.12 (.78)	.10 (.67)	1
0 - 0.5	.96-1.0	-16 to +16	.84 (1.6)	.19 (.65)	.43 (1.1)	.12 (.61)	.10 (.49)	.09 (.48)	0
0 - 0.5	.96-1.0	-2 to +16	1.0 (1.5)	.21 (.49)	.52 (.95)	.08 (.37)	.09 (.36)	.09 (.36)	1
0 - 0.5	.96-1.0	-16 to +2	.58 (1.0)	.12 (.44)	.29 (.74)	.08 (.44)	.06 (.33)	.06 (.30)	1
0.5 - 1	.96-1.0	-16 to +16	.76 (1.9)	.26 (.73)	.42 (1.1)	.19 (.95)	.13 (.68)	.11 (.60)	0
0.5 - 1	.96-1.0	-2 to +16	.88 (1.8)	.31 (.75)	.47 (1.1)	.12 (.59)	.10 (.39)	.09 (.35)	1
0.5 - 1	.96-1.0	-16 to +2	.54 (1.2)	.16 (.54)	.28 (.72)	.19 (.82)	.11 (.56)	.09 (.48)	1
1 - 2	.96-1.0	-16 to +16	.86 (3.6)	.40 (1.5)	.45 (1.2)	.51 (2.7)	.28 (1.5)	.23 (1.3)	0
1 - 2	.96-1.0	-2 to +16	.83 (2.0)	.41 (1.5)	.47 (1.3)	.29 (1.6)	.18 (1.0)	.16 (.83)	1
1 - 2	.96-1.0	-16 to +2	.74 (3.4)	.33 (1.4)	.34 (.96)	.59 (2.7)	.31 (1.5)	.24 (1.2)	1
1 - 1.5	.96-1.0	-16 to +16	.66 (1.8)	.31 (.88)	.39 (1.0)	.27 (1.2)	.16 (.77)	.14 (.69)	0
1 - 1.5	.96-1.0	-2 to +16	.71 (1.5)	.36 (.91)	.41 (1.1)	.16 (.76)	.12 (.50)	.10 (.43)	1
1 - 1.5	.96-1.0	-16 to +2	.50 (1.7)	.21 (.60)	.26 (.70)	.30 (1.1)	.16 (.69)	.13 (.61)	1
1.5 - 2	.96-1.0	-16 to +16	.76 (2.9)	.35 (.92)	.42 (1.1)	.37 (1.6)	.20 (.87)	.17 (.74)	0
1.5 - 2	.96-1.0	-2 to +16	.66 (1.7)	.39 (1.1)	.41 (1.2)	.21 (.95)	.13 (.59)	.12 (.51)	1
1.5 - 2	.96-1.0	-16 to +2	.68 (2.8)	.25 (.70)	.32 (.88)	.43 (1.5)	.22 (.80)	.17 (.68)	1
0 - 1	.91-.95	-16 to +16	.80 (1.9)	.23 (1.0)	.42 (1.2)	.23 (1.5)	.16 (1.1)	.15 (.96)	0
0 - 1	.91-.95	-2 to +16	.96 (1.8)	.25 (.86)	.49 (1.1)	.15 (.94)	.12 (.64)	.11 (.59)	1
0 - 1	.91-.95	-16 to +2	.54 (1.5)	.17 (.83)	.27 (.83)	.23 (1.2)	.15 (.89)	.13 (.80)	1
0 - 0.5	.91-.95	-16 to +16	.80 (1.6)	.18 (.76)	.41 (1.2)	.13 (.69)	.11 (.58)	.10 (.55)	0
0 - 0.5	.91-.95	-2 to +16	.97 (1.5)	.20 (.58)	.49 (1.0)	.09 (.45)	.09 (.43)	.08 (.42)	1
0 - 0.5	.91-.95	-16 to +2	.52 (.99)	.12 (.50)	.26 (.89)	.10 (.50)	.07 (.39)	.07 (.36)	1
0.5 - 1	.91-.95	-16 to +16	.74 (1.9)	.25 (.72)	.40 (1.1)	.21 (1.0)	.15 (.78)	.13 (.71)	0
0.5 - 1	.91-.95	-2 to +16	.85 (1.7)	.29 (.72)	.46 (1.0)	.13 (.67)	.10 (.47)	.09 (.42)	1
0.5 - 1	.91-.95	-16 to +2	.50 (1.2)	.16 (.56)	.26 (.74)	.21 (.83)	.13 (.63)	.12 (.58)	1
1 - 2	.91-.95	-16 to +16	.88 (4.0)	.42 (1.6)	.46 (1.3)	.60 (3.1)	.34 (1.8)	.28 (1.5)	0
1 - 2	.91-.95	-2 to +16	.82 (2.4)	.41 (1.6)	.46 (1.3)	.34 (1.9)	.21 (1.2)	.18 (1.0)	1
1 - 2	.91-.95	-16 to +2	.82 (3.9)	.39 (1.5)	.38 (1.2)	.70 (2.9)	.38 (1.6)	.31 (1.3)	1
1 - 1.5	.91-.95	-16 to +16	.66 (2.0)	.31 (.96)	.38 (1.1)	.31 (1.3)	.19 (.86)	.17 (.80)	0
1 - 1.5	.91-.95	-2 to +16	.70 (1.5)	.34 (.86)	.40 (1.1)	.19 (.88)	.12 (.60)	.11 (.53)	1
1 - 1.5	.91-.95	-16 to +2	.50 (1.9)	.22 (.71)	.26 (.69)	.34 (1.1)	.20 (.76)	.17 (.70)	1
1.5 - 2	.91-.95	-16 to +16	.81 (3.3)	.35 (1.0)	.43 (1.2)	.44 (1.8)	.25 (.99)	.21 (.86)	0
1.5 - 2	.91-.95	-2 to +16	.67 (2.1)	.37 (1.0)	.40 (1.2)	.25 (1.2)	.16 (.72)	.13 (.63)	1
1.5 - 2	.91-.95	-16 to +2	.79 (3.2)	.29 (.89)	.37 (1.1)	.51 (1.7)	.27 (.91)	.22 (.79)	1

TABLE 4. The dependence of errors in the θ_v-dependent split-window LST algorithm on the range of the atmospheric lower boundary temperature (T_{air-sf}) in warm atmospheric conditions for the higher emissivity group.

application ranges			$300°K \leq T_{air-sf} \leq 310°K$			$300°K \leq T_{air-sf} \leq 305°K$			max
vwv (cm)	ε_5	$T_s - T_{air-sf}$	$\theta_v = 69°$	$\theta_v = 45°$	$\theta_v = 0°$	$\theta_v = 69°$	$\theta_v = 45°$	$\theta_v = 0°$	$(T_s - T_4)$
2 - 2.5	.96-1.0	+7 to +16	.73 (2.2)	.53 (1.5)	.42 (1.2)	.78 (2.1)	.55 (1.5)	.44 (1.2)	17.3 °K
2 - 2.5	.96-1.0	-2 to +9.5	.61 (2.1)	.41 (1.4)	.32 (1.1)	.65 (2.0)	.41 (1.3)	.31 (.96)	14.4 °K
2 - 2.5	.96-1.0	-9.5 to +2	.46 (1.6)	.29 (1.0)	.22 (.86)	.45 (1.5)	.26 (.83)	.19 (.64)	11.0 °K
2 - 2.5	.96-1.0	-16 to -7	.37 (1.5)	.22 (1.1)	.18 (.89)	.34 (1.4)	.20 (.89)	.16 (.74)	6.7 °K
2.5 - 3	.96-1.0	+7 to +16	.76 (2.4)	.59 (1.8)	.48 (1.5)	.83 (2.3)	.62 (1.7)	.51 (1.4)	19.8 °K
2.5 - 3	.96-1.0	-2 to +9.5	.67 (2.4)	.48 (1.6)	.38 (1.3)	.71 (2.3)	.48 (1.5)	.37 (1.2)	16.3 °K
2.5 - 3	.96-1.0	-9.5 to +2	.53 (1.8)	.35 (1.2)	.27 (1.0)	.52 (1.7)	.31 (1.0)	.23 (.76)	12.2 °K
2.5 - 3	.96-1.0	-16 to -7	.44 (1.7)	.27 (1.2)	.22 (1.0)	.38 (1.5)	.23 (1.0)	.18 (.83)	7.2 °K
3 - 3.5	.96-1.0	+7 to +16	.83 (2.6)	.63 (2.0)	.54 (1.7)	.88 (2.4)	.68 (1.9)	.57 (1.6)	22.4 °K
3 - 3.5	.96-1.0	-2 to +9.5	.77 (2.7)	.53 (1.9)	.44 (1.5)	.77 (2.5)	.54 (1.8)	.43 (1.4)	18.3 °K
3 - 3.5	.96-1.0	-9.5 to +2	.62 (2.1)	.41 (1.4)	.32 (1.2)	.57 (1.8)	.37 (1.2)	.28 (.93)	13.6 °K
3 - 3.5	.96-1.0	-16 to -7	.50 (1.9)	.32 (1.3)	.25 (1.2)	.42 (1.7)	.25 (1.1)	.20 (.88)	7.7 °K
3.5 - 4	.96-1.0	+7 to +16	1.0 (2.8)	.67 (2.1)	.58 (1.8)	.95 (2.7)	.72 (2.0)	.62 (1.8)	24.9 °K
3.5 - 4	.96-1.0	-2 to +9.5	1.0 (3.1)	.58 (2.1)	.49 (1.7)	.83 (2.7)	.60 (1.9)	.49 (1.6)	20.3 °K
3.5 - 4	.96-1.0	-9.5 to +2	.84 (2.4)	.46 (1.6)	.37 (1.3)	.63 (2.0)	.42 (1.4)	.33 (1.1)	14.9 °K
3.5 - 4	.96-1.0	-16 to -7	.58 (2.2)	.37 (1.4)	.29 (1.2)	.48 (1.8)	.28 (1.1)	.21 (.93)	8.4 °K
4 - 4.5	.96-1.0	+7 to +16	1.4 (3.2)	.71 (2.3)	.62 (2.0)	1.1 (2.9)	.77 (2.1)	.67 (1.9)	27.2 °K
4 - 4.5	.96-1.0	-2 to +9.5	1.5 (3.9)	.64 (2.3)	.54 (1.9)	.93 (3.0)	.65 (2.1)	.54 (1.8)	22.2 °K
4 - 4.5	.96-1.0	-9.5 to +2	1.2 (3.5)	.51 (1.7)	.42 (1.4)	.72 (2.2)	.47 (1.5)	.37 (1.2)	16.3 °K
4 - 4.5	.96-1.0	-16 to -7	.76 (2.4)	.41 (1.6)	.33 (1.3)	.56 (2.0)	.30 (1.2)	.23 (.98)	9.1 °K
4.5 - 5	.96-1.0	+7 to +16	1.9 (4.4)	.77 (2.3)	.66 (2.0)	1.2 (3.2)	.81 (2.2)	.70 (1.9)	29.4 °K
4.5 - 5	.96-1.0	-2 to +9.5	2.1 (5.6)	.72 (2.4)	.58 (2.0)	1.1 (3.4)	.69 (2.2)	.58 (1.8)	24.0 °K
4.5 - 5	.96-1.0	-9.5 to +2	1.8 (5.1)	.58 (1.9)	.46 (1.5)	.87 (2.5)	.51 (1.6)	.41 (1.3)	17.6 °K
4.5 - 5	.96-1.0	-16 to -7	1.1 (3.6)	.45 (1.7)	.36 (1.5)	.68 (2.0)	.33 (1.2)	.25 (.96)	10.0 °K

TABLE 5. The dependence of errors in the θ_V-dependent split-window LST algorithm on the range of the atmospheric lower boundary temperature (T_{air-sf}) in warm atmospheric conditions for the lower emissivity group.

application ranges			$300°K \leq T_{air-sf} \leq 310°K$			$300°K \leq T_{air-sf} \leq 305°K$			max
vwv (cm)	ε_5	$T_s - T_{air-sf}$	$\theta_V = 69°$	$\theta_V = 45°$	$\theta_V = 0°$	$\theta_V = 69°$	$\theta_V = 45°$	$\theta_V = 0°$	$(T_s - T_4)$
2 - 2.5	.91-.95	+7 to +16	.67 (2.1)	.45 (1.4)	.34 (1.1)	.72 (2.0)	.47 (1.4)	.35 (1.0)	19.1 °K
2 - 2.5	.91-.95	-2 to +9.5	.54 (2.0)	.33 (1.2)	.24 (1.0)	.55 (1.9)	.31(1.1)	.21 (.74)	16.1 °K
2 - 2.5	.91-.95	-9.5 to +2	.42 (1.6)	.24 (1.1)	.19 (.97)	.37 (1.3)	.20 (.86)	.16 (.76)	12.5 °K
2 - 2.5	.91-.95	-16 to -7	.49 (2.0)	.34 (1.4)	.29 (1.2)	.48 (1.9)	.33 (1.3)	.29 (1.1)	8.2 °K
2.5 - 3	.91-.95	+7 to +16	.72 (2.4)	.52 (1.7)	.41 (1.4)	.77 (2.2)	.54 (1.6)	.42 (1.3)	21.3 °K
2.5 - 3	.91-.95	-2 to +9.5	.61 (2.3)	.40 (1.5)	.31 (1.2)	.63 (2.1)	.38 (1.4)	.27 (.97)	17.7 °K
2.5 - 3	.91-.95	-9.5 to +2	.49 (1.8)	.30 (1.4)	.24 (1.1)	.44 (1.5)	.25 (.93)	.18 (.82)	13.4 °K
2.5 - 3	.91-.95	-16 to -7	.57 (2.2)	.39 (1.5)	.33 (1.3)	.51 (2.0)	.35 (1.4)	.30 (1.2)	8.1 °K
3 - 3.5	.91-.95	+7 to +16	.79 (2.6)	.58 (1.9)	.47 (1.6)	.83 (2.4)	.61 (1.8)	.49 (1.5)	23.5 °K
3 - 3.5	.91-.95	-2 to +9.5	.72 (2.7)	.47 (1.8)	.37 (1.4)	.69 (2.4)	.45 (1.6)	.34 (1.2)	19.3 °K
3 - 3.5	.91-.95	-9.5 to +2	.58 (2.0)	.36 (1.5)	.29 (1.3)	.51 (1.7)	.30 (1.0)	.22 (.84)	14.4 °K
3 - 3.5	.91-.95	-16 to -7	.64 (2.5)	.43 (1.7)	.37 (1.4)	.53 (2.1)	.36 (1.5)	.31 (1.3)	8.4 °K
3.5 - 4	.91-.95	+7 to +16	.98 (2.8)	.62 (2.1)	.53 (1.8)	.89 (2.6)	.66 (2.0)	.55 (1.7)	25.7 °K
3.5 - 4	.91-.95	-2 to +9.5	.95 (3.1)	.53 (2.0)	.43 (1.6)	.76 (2.6)	.51 (1.8)	.40 (1.4)	21.0 °K
3.5 - 4	.91-.95	-9.5 to +2	.76 (2.4)	.42 (1.7)	.34 (1.5)	.58 (1.9)	.35 (1.2)	.26 (.89)	15.5 °K
3.5 - 4	.91-.95	-16 to -7	.68 (2.7)	.49 (2.0)	.40 (1.6)	.58 (2.2)	.37 (1.5)	.31 (1.3)	8.9 °K
4 - 4.5	.91-.95	+7 to +16	1.4 (3.4)	.67 (2.3)	.57 (1.9)	1.0 (2.9)	.71 (2.1)	.60 (1.8)	27.8 °K
4 - 4.5	.91-.95	-2 to +9.5	1.4 (4.1)	.58 (2.2)	.48 (1.8)	.86 (2.9)	.57 (2.0)	.46 (1.6)	22.7 °K
4 - 4.5	.91-.95	-9.5 to +2	1.1 (3.5)	.47 (1.7)	.39 (1.6)	.67 (2.1)	.40 (1.4)	.31 (1.1)	16.7 °K
4 - 4.5	.91-.95	-16 to -7	.77 (2.8)	.54 (2.3)	.45 (1.9)	.65 (2.4)	.37 (1.6)	.31 (1.3)	9.5 °K
4.5 - 5	.91-.95	+7 to +16	1.9 (4.6)	.73 (2.4)	.61 (2.0)	1.2 (3.2)	.75 (2.2)	.64 (1.9)	29.8 °K
4.5 - 5	.91-.95	-2 to +9.5	2.0 (5.7)	.67 (2.4)	.53 (2.0)	1.0 (3.3)	.62 (2.1)	.51 (1.7)	24.3 °K
4.5 - 5	.91-.95	-9.5 to +2	1.7 (5.1)	.54 (1.8)	.43 (1.6)	.82 (2.4)	.45 (1.5)	.35 (1.2)	17.9 °K
4.5 - 5	.91-.95	-16 to -7	1.1 (3.3)	.57 (2.5)	.47 (2.1)	.75 (2.3)	.38 (1.5)	.30 (1.2)	10.2 °K

TABLE 6. The maximum emissivity sensitivitiies (α, β) of split-window LST algorithms in cold and dry atmospheric conditions ($T_{air-sf} \leq 287.2$ °K and vertical column water vapor < 2cm).

application ranges			θ_V-independent LST method			θ_V-dependent LST method			iteration
vwv (cm)	ε_5	$T_s - T_{air-sf}$	$\theta_V = 69°$	$\theta_V = 45°$	$\theta_V = 0°$	$\theta_V = 69°$	$\theta_V = 45°$	$\theta_V = 0°$	number
0 - 1	.96-1.0	-16 to +16	58, -116	57, -117	56, -117	58, -128	58, -89	58, -80	0
0 - 1	.96-1.0	-2 to +16	57, -133	56, -134	56, -134	57, -117	58, -101	58, -93	1
0 - 1	.96-1.0	-16 to +2	52, -90	52, -91	52, -91	53, -94	53, -74	53, -65	1
0 - 0.5	.96-1.0	-16 to +16	57, -94	57, -94	57, -94	57, -95	58, -74	58, -66	0
0 - 0.5	.96-1.0	-2 to +16	57, -105	57, -105	57, -105	58, -102	59, -85	59, -77	1
0 - 0.5	.96-1.0	-16 to +2	52, -79	52, -79	52, -79	52, -90	53, -68	54, -59	1
0.5 - 1	.96-1.0	-16 to +16	59, -139	57, -139	57, -139	61, -107	59, -85	59, -74	0
0.5 - 1	.96-1.0	-2 to +16	57, -155	56, -156	55, -157	58, -106	58, -89	58, -79	1
0.5 - 1	.96-1.0	-16 to +2	52, -102	52, -103	52, -103	54, -95	53, -75	53, -66	1
1 - 2	.96-1.0	-16 to +16	62, -117	59, -116	57, -116	61, -97	60, -95	60, -90	0
1 - 2	.96-1.0	-2 to +16	57, -129	55, -136	54, -138	55, -104	56, -95	56, -89	1
1 - 2	.96-1.0	-16 to +2	53, -89	52, -90	51, -90	53, -80	53, -76	52, -72	1
1 - 1.5	.96-1.0	-16 to +16	62, -144	59, -141	57, -139	62, -114	61, -98	60, -87	0
1 - 1.5	.96-1.0	-2 to +16	59, -144	57, -148	56, -149	59, -100	58, -90	58, -83	1
1 - 1.5	.96-1.0	-16 to +2	53, -106	52, -105	52, -105	55, -96	53, -84	52, -75	1
1.5 - 2	.96-1.0	-16 to +16	61, -128	58, -123	56, -121	60, -107	60, -101	60, -94	0
1.5 - 2	.96-1.0	-2 to +16	58, -120	55, -125	54, -127	57, -93	57, -89	57, -84	1
1.5 - 2	.96-1.0	-16 to +2	52, -89	51, -88	50, -88	52, -87	52, -86	52, -80	1
0 - 1	.91-.95	-16 to +16	56, -113	55, -114	54, -114	57, -104	56, -85	56, -75	0
0 - 1	.91-.95	-2 to +16	55, -124	54, -125	54, -125	56, -107	56, -88	56, -76	1
0 - 1	.91-.95	-16 to +2	50, -95	50, -96	49, -96	50, -108	50, -84	50, -74	1
0 - 0.5	.91-.95	-16 to +16	54, -83	55, -84	55, -84	55, -91	56, -68	56, -59	0
0 - 0.5	.91-.95	-2 to +16	55, -92	55, -93	55, -93	56, -96	56, -77	57, -68	1
0 - 0.5	.91-.95	-16 to +2	50, -72	50, -72	50, -72	50, -91	51, -65	51, -55	1
0.5 - 1	.91-.95	-16 to +16	56, -133	54, -132	54, -131	58, -109	56, -85	56, -73	0
0.5 - 1	.91-.95	-2 to +16	55, -145	54, -146	53, -147	56, -98	56, -78	56, -68	1
0.5 - 1	.91-.95	-16 to +2	50, -101	49, -101	49, -101	51, -109	50, -85	50, -75	1
1 - 2	.91-.95	-16 to +16	61, -118	57, -116	55, -115	59, -97	58, -96	57, -93	0
1 - 2	.91-.95	-2 to +16	58, -119	56, -124	54, -126	55, -94	55, -83	55, -76	1
1 - 2	.91-.95	-16 to +2	54, -92	51, -93	50, -93	54, -87	52, -92	50, -90	1
1 - 1.5	.91-.95	-16 to +16	59, -141	56, -137	55, -135	59, -115	57, -99	56, -88	0
1 - 1.5	.91-.95	-2 to +16	58, -135	55, -137	54, -138	56, -95	56, -84	55, -76	1
1 - 1.5	.91-.95	-16 to +2	51, -107	50, -107	50, -106	52, -105	50, -93	50, -85	1
1.5 - 2	.91-.95	-16 to +16	59, -123	55, -119	54, -116	58, -106	57, -102	56, -96	0
1.5 - 2	.91-.95	-2 to +16	57, -111	55, -115	53, -117	56, -88	55, -84	54, -79	1
1.5 - 2	.91-.95	-16 to +2	51, -88	49, -87	49, -87	51, -88	50, -91	49, -87	1

TABLE 7. The maximum emissivity sensitivities (α, β) of split-window LST algorithms in warm atmospheric conditions (294 °K ≤ T_{air-sf} ≤ 300 °K).

application ranges			θ_V-independent LST method			θ_V-dependent LST method			iteration
vwv (cm)	ε_5	$T_s - T_{air-sf}$	$\theta_V = 69°$	$\theta_V = 45°$	$\theta_V = 0°$	$\theta_V = 69°$	$\theta_V = 45°$	$\theta_V = 0°$	number
0 - 0.5	.96-1.0	-16 to +16	61, -111	61, -112	61, -112	61, -109	62, -84	63, -72	0
0 - 0.5	.96-1.0	-2 to +16	61, -121	61, -121	61, -121	62, -115	63, -95	64, -84	1
0 - 0.5	.96-1.0	-16 to +2	56, -104	56, -104	56, -105	55, -114	57, -85	58, -73	1
0.5 - 1	.96-1.0	-16 to +16	62, -161	61, -161	60, -161	65, -114	63, -95	63, -84	0
0.5 - 1	.96-1.0	-2 to +16	61, -179	59, -180	59, -181	62, -117	63, -101	63, -92	1
0.5 - 1	.96-1.0	-16 to +2	56, -125	55, -125	55, -126	57, -105	57, -87	57, -77	1
1 - 1.5	.96-1.0	-16 to +16	65, -160	62, -158	61, -157	66, -121	65, -104	64, -93	0
1 - 1.5	.96-1.0	-2 to +16	63, -167	60, -171	59, -172	63, -111	62, -100	62, -92	1
1 - 1.5	.96-1.0	-16 to +2	57, -120	56, -120	56, -120	58, -102	57, -90	56, -82	1
1.5 - 2	.96-1.0	-16 to +16	65, -141	62, -138	60, -136	65, -117	64, -110	64, -100	0
1.5 - 2	.96-1.0	-2 to +16	62, -139	59, -146	58, -149	62, -104	61, -98	61, -93	1
1.5 - 2	.96-1.0	-16 to +2	56, -98	55, -99	54, -99	57, -94	56, -90	55, -84	1
2 - 2.5	.96-1.0	-16 to +16	62, -120	59, -117	58, -115	62, -107	63, -106	62, -102	0
2 - 2.5	.96-1.0	-2 to +16	58, -119	57, -124	56, -126	59, -97	60, -95	59, -91	1
2 - 2.5	.96-1.0	-16 to +2	52, -76	50, -77	49, -78	53, -82	54, -85	54, -82	1
2.5 - 3	.96-1.0	-16 to +16	57, -101	56, -98	54, -96	60, -93	60, -98	60, -98	0
2.5 - 3	.96-1.0	-2 to +16	53, -101	53, -106	52, -108	57, -87	57, -90	57, -88	1
2.5 - 3	.96-1.0	-16 to +2	45, -59	44, -60	43, -61	49, -68	51, -77	51, -77	1
3 - 3.5	.96-1.0	-16 to +16	52, -84	51, -82	50, -80	56, -78	57, -88	57, -90	0
3 - 3.5	.96-1.0	-2 to +16	48, -84	49, -89	49, -91	54, -75	54, -82	54, -82	1
3 - 3.5	.96-1.0	-16 to +2	37, -46	37, -47	37, -47	44, -55	47, -66	47, -68	1

TABLE 8. The maximum sensitivity (°K) of the θ_V-dependent LST algorithm to the instrument noise in warm atmospheric conditions (294 °K ≤ T_{air-sf} ≤ 300 °K).

application ranges vwv (cm)	ε_5	10-bit quantization $\Delta RMS(\delta T_s)$	10-bit quantization $\Delta\max(\delta T_s)$	9-bit quantization $\Delta RMS(\delta T_s)$	9-bit quantization $\Delta\max(\delta T_s)$
0 - 0.5	.96-1.0	0.07 °K	0.16 °K	0.18 °K	0.48 °K
0.5 - 1	.96-1.0	0.05 °K	0.12 °K	0.13 °K	0.35 °K
1 - 1.5	.96-1.0	0.04 °K	0.17 °K	0.12 °K	0.32 °K
1.5 - 2	.96-1.0	0.04 °K	0.15 °K	0.12 °K	0.29 °K
2 - 2.5	.96-1.0	0.05 °K	0.20 °K	0.14 °K	0.33 °K
2.5 - 3	.96-1.0	0.07 °K	0.23 °K	0.19 °K	0.49 °K
3 - 3.5	.96-1.0	0.08 °K	0.23 °K	0.23 °K	0.58 °K
0 - 0.5	.91-.95	0.08 °K	0.28 °K	0.22 °K	0.66 °K
0.5 - 1	.91-.95	0.06 °K	0.40 °K	0.19 °K	0.62 °K
1 - 1.5	.91-.95	0.04 °K	0.30 °K	0.16 °K	0.71 °K
1.5 - 2	.91-.95	0.04 °K	0.20 °K	0.13 °K	0.56 °K
2 - 2.5	.91-.95	0.05 °K	0.21 °K	0.15 °K	0.45 °K
2.5 - 3	.91-.95	0.05 °K	0.22 °K	0.17 °K	0.57 °K
3 - 3.5	.91-.95	0.06 °K	0.30 °K	0.22 °K	0.58 °K

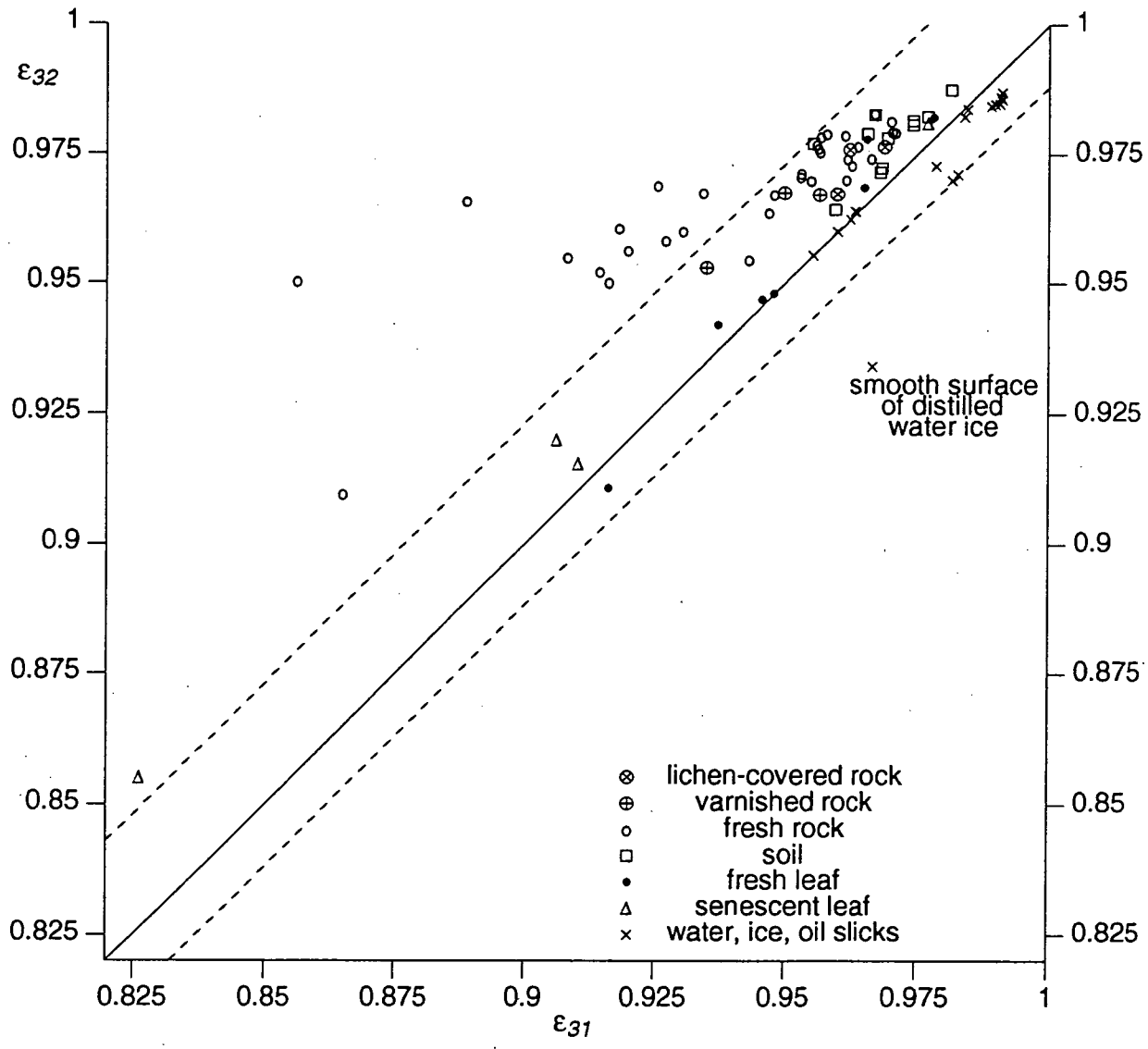

Figure 1. Band averaged emissivities of terrestrial materials for MODIS bands 31 and 32.

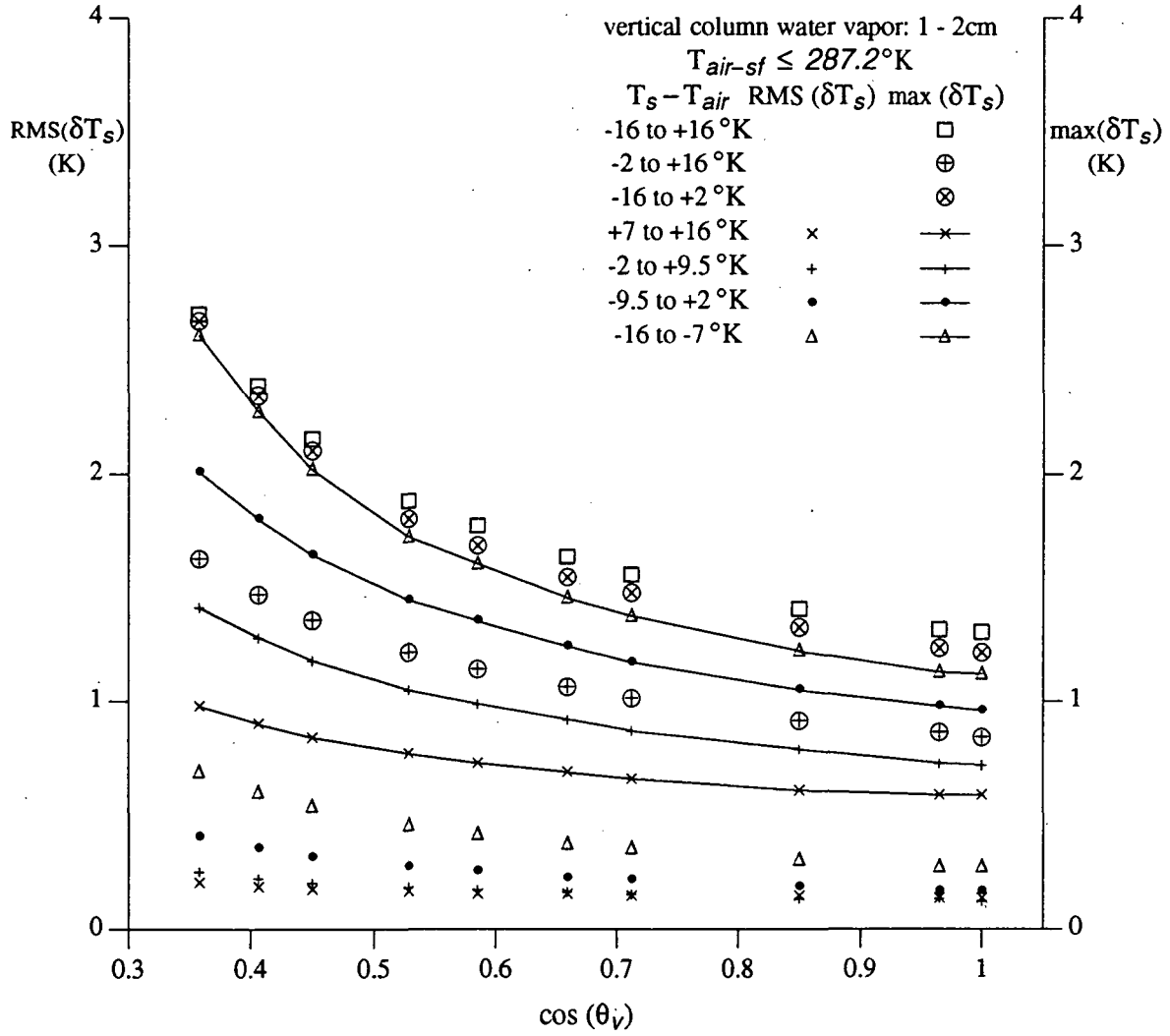

Figure 2. The RMS and maximum errors of the generalized LST algorithm versus viewing angle in cold and dry atmospheric conditions for the higher emissivity group.

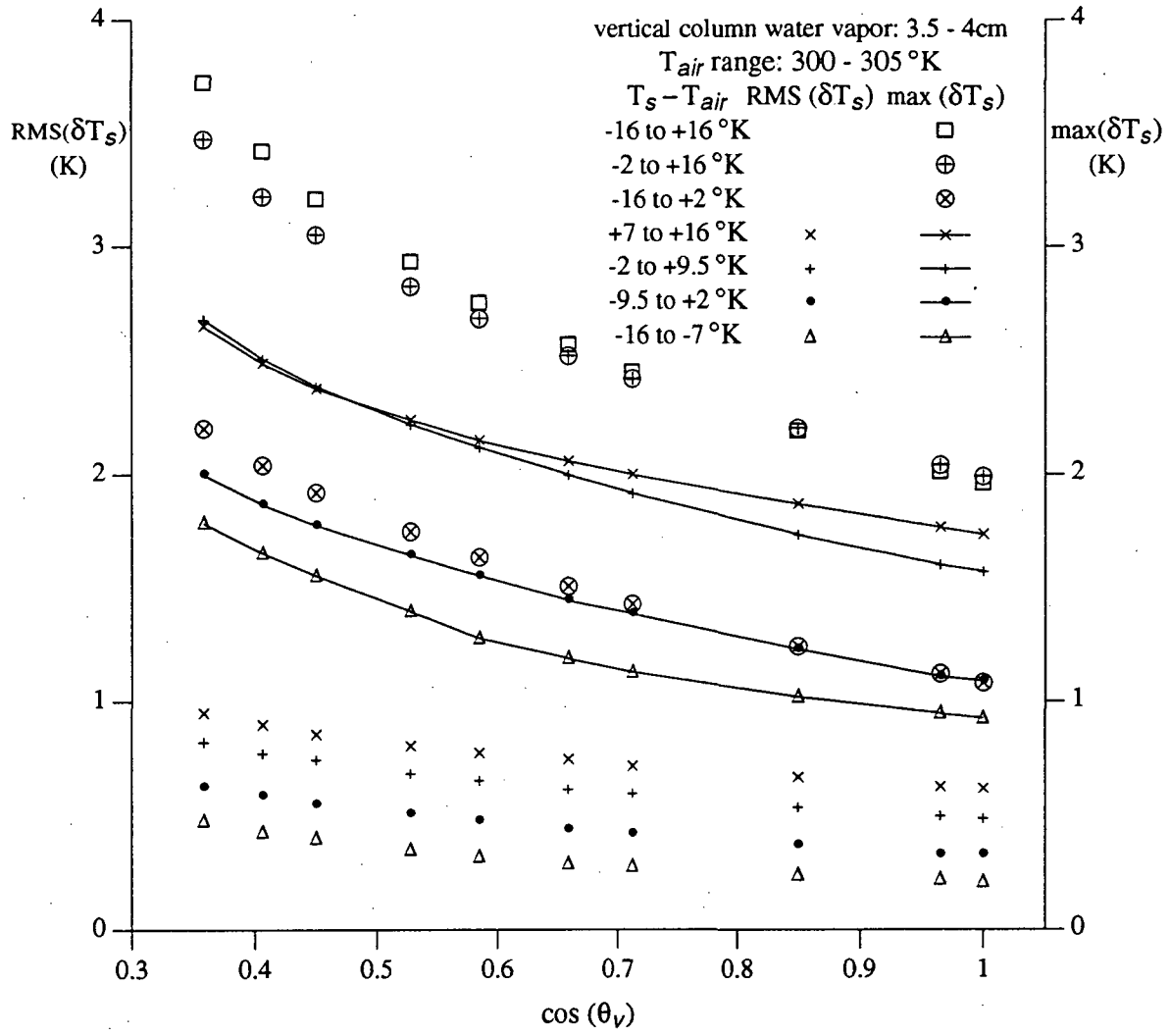

Figure 3. The RMS and maximum errors of the generalized LST algorithm versus viewing angle in warm and wet atmospheric conditions for the higher emissivity group.

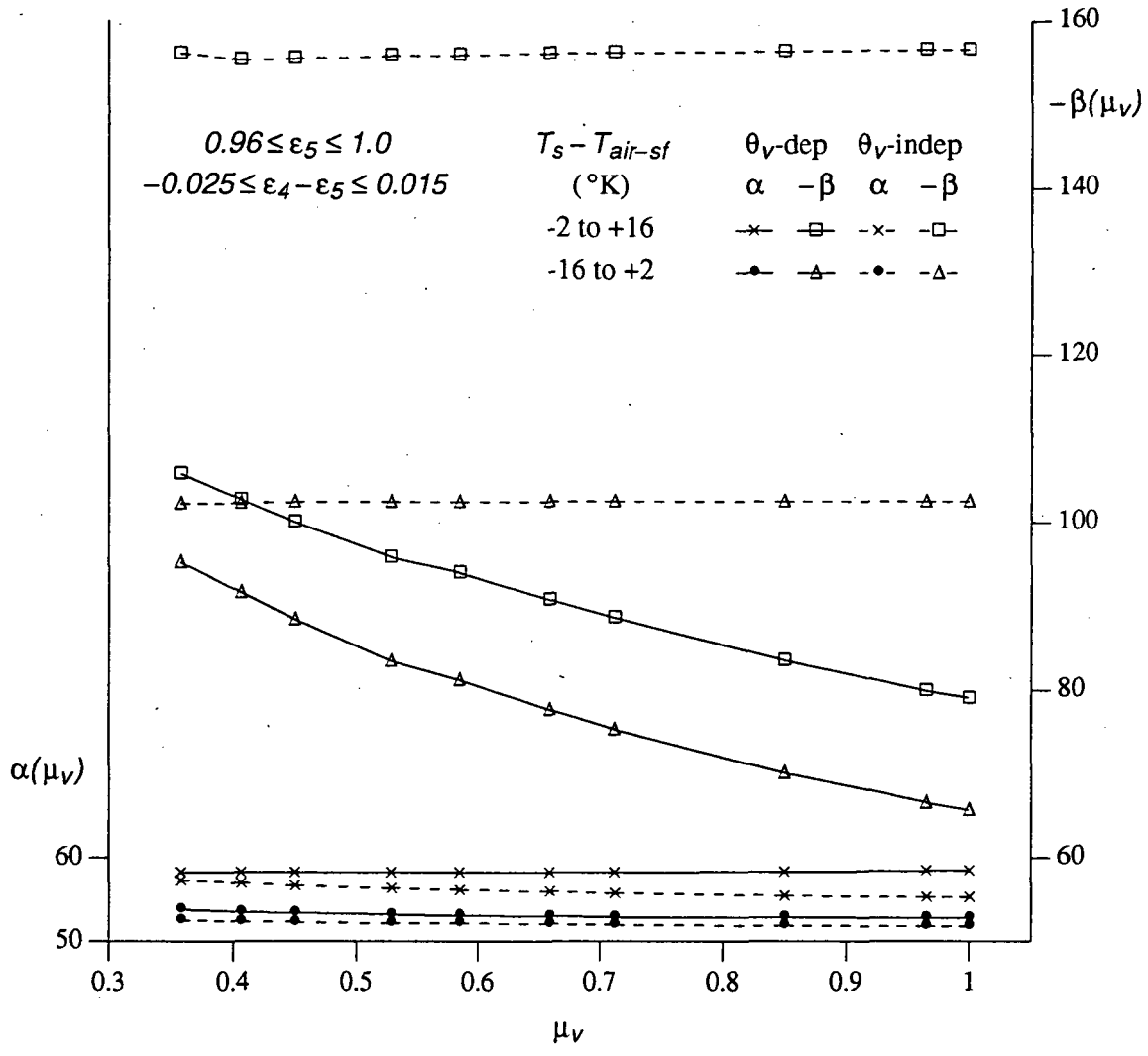

Figure 4. The maximum sensitivities of emissivity variations in the generalized LST algorithms in relatively cold atmospheric conditions ($T_{air-sf} \leq 287.2$ °K and water vapor in 0.5-1cm).

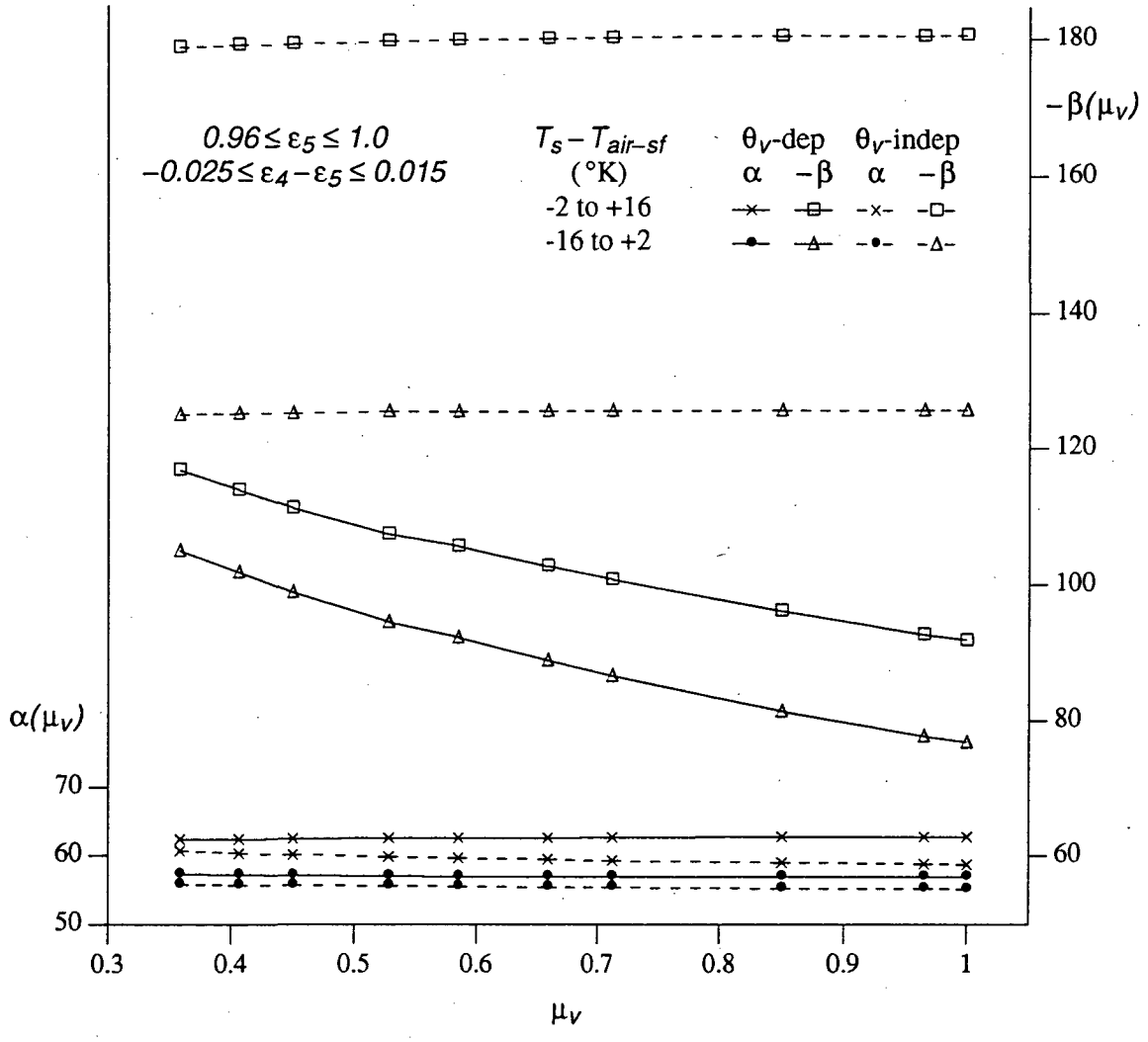

Figure 5. The maximum sensitivities of emissivity variations in the generalized LST algorithms in warm atmospheric conditions ($294\,°K \le T_{air-sf} \le 300\,°K$ and water vapor in 0.5-1cm).

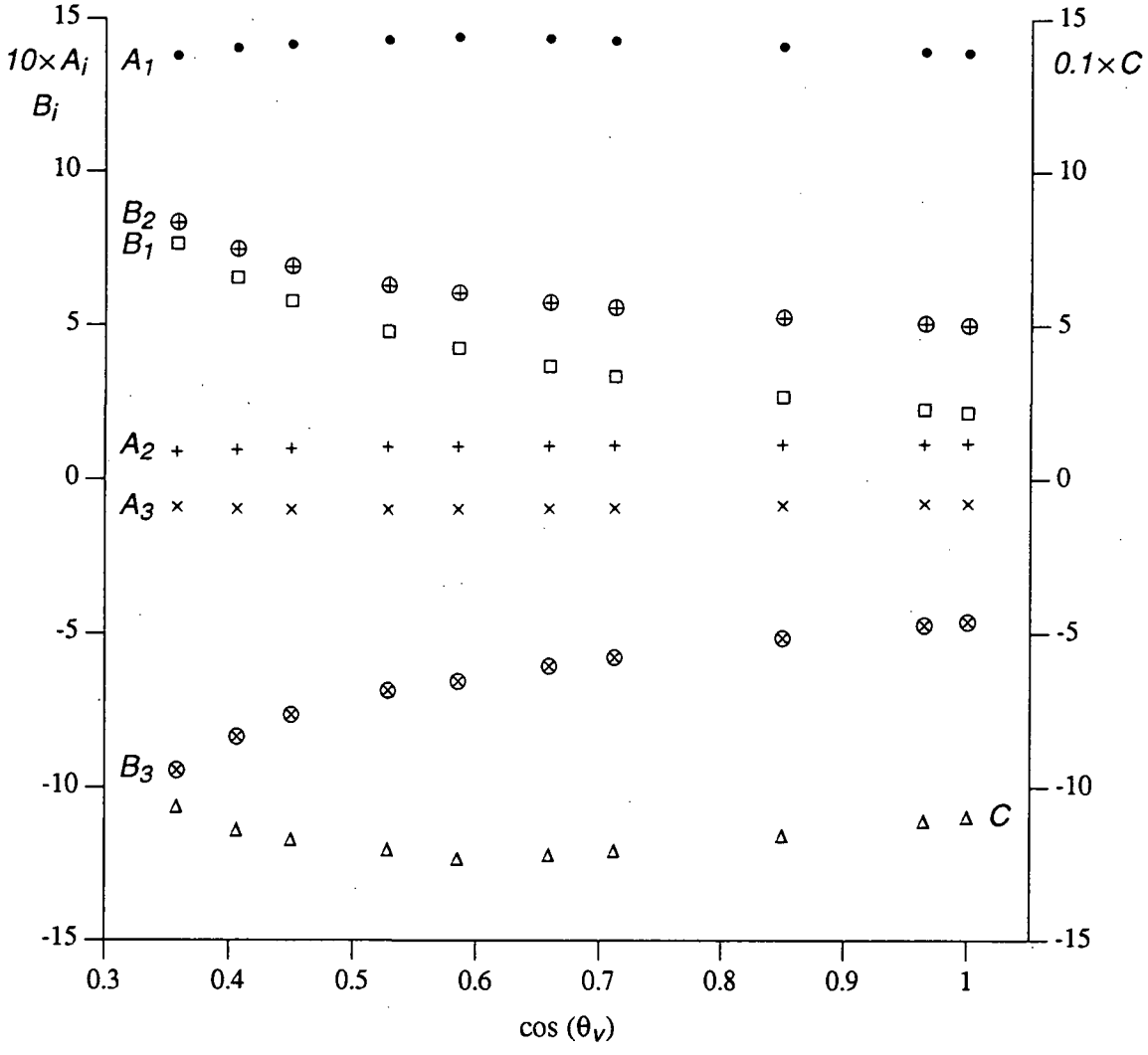

Figure 6. The coefficients of the generalized LST algorithm for the higher emissivity group in the ranges of T_{air-sf} 300-305K, water vapor 3.5-4cm and $-2°K \leq T_s - T_{air-sf} \leq 9.5°K$.